Title:

Effect of additional magnesium on mechanical and high-cycle fatigue properties of 6061–T6 alloy

Authors & Affiliations:

Yoshimasa TAKAHASHI [a,*], Takahiro SHIKAMA [b], Ryota NAKAMICHI [a], Yuji KAWATA [a], Naoki KASAGI [a,**], Hironari NISHIOKA [a], Syuzaburo KITA [a], Masanori TAKUMA [a], Hiroshi NOGUCHI [c]

[a] *Department of Mechanical Engineering, Kansai University, 3-3-35 Yamate-cho, Suita-shi, Osaka 564-8680, Japan*

[b] *Kobe Steel Ltd., Aluminum & Copper Business (Chofu Works), 14-1 Chofu Minato-machi, Shimonoseki,Yamaguchi 752-0953, Japan*

[c] *Department of Mechanical Engineering, Kyushu University, 744 Motooka, Nishi-ku, Fukuoka 819-0395, Japan*

[*] Corresponding author

Tel: +81-6-6368-0748

E-mail: yoshim-t@kansai-u.ac.jp

[**] Currently at Suzuki Motor Corporation Ltd.

Abstract:

The effect of additional solute magnesium (Mg) on mechanical and high-cycle-fatigue properties of 6061-T6 aluminum alloy is investigated in detail. By adding 0.5% and 0.8% Mg to the 6061-T6 alloy with a normal stoichiometric Mg_2Si composition (base alloy), the alloy exhibits eminent strain-aging characteristics demonstrated by the emergence of serrated flow, the negative

strain-rate-sensitivity and relatively weakened temperature dependency of flow stress. The Mg-added new alloy also shows higher work-hardening rate than the base alloy particularly at initial flow regime and at lower strain rate. The *S-N* curve of the new alloy shows a clear fatigue limit which is absent in the base alloy. The fatigue limit of the new alloy is shown to be controlled by the threshold against small crack growth. Moreover, the new alloy clearly exhibits a coaxing phenomenon (time-dependent strengthening) which is absent in the base alloy. The coaxing effect is attributed to the existence of a small quasi-non-propagating crack whose growth resistance gradually increases during stress amplitude step-ups.

Key words:

6061-T6 alloys; Solute magnesium; Work-hardening; Strain-aging; Fatigue limit; Coaxing effect

Main text:

1. Introduction

The growing need for weight reduction of structural components has remarkably increased the demand for high strength Aluminum (Al) alloys over the past decade particularly in automobile or railroad industries. The 6061 alloy, a representative Al-Mg-Si (6XXX) alloy, is one of such material class whose matrix can be age-hardened with precipitates of magnesium-silicide (Mg_2Si) [1]. Despite its high specific strength, the high-cycle-fatigue (HCF) property of artificially aged 6061 (6061-T6) is inferior to conventional ferrous alloys in terms of fatigue limit; the stress-life (*S-N*) curve of 6061-T6 shows no distinct knee-point around 10^5-10^6 cycles [1-4] like other non-ferrous pure face-centered-cubic (FCC) alloys. The absence of a clear threshold in HCF regime hence necessitates the introduction of a finite life strength (typically at $5 \times 10^7 \sim 10^8$ cycles for Al alloys [5]) to fatigue design, which has long been accepted as an inevitable engineering compromise while the cost of data acquisition is monumental.

In order to change such a longstanding paradigm, several of the authors began to develop a new 6061-based prototype alloy and investigated its HCF property [6,7]. The concept of the new alloy was to artificially control the appearance of a distinct fatigue limit through the addition of a strain-aging capability. Such an idea originally came from a well-known classical theory regarding the fatigue limit in ferrous alloys containing interstitials such as carbon (C) or nitrogen (N) [8-11]. Since possible interstitials (e.g. boron (B), C, N) were known to show hardly any solubility in Al matrix at room temperature [12], the addition of strain-aging capability to 6061-T6 alloy had to be achieved in a different way. Then it was found that the addition of small amount of substitutional element (Mg) to the normal 6061-T6 alloy with a stoichiometric Mg_2Si composition successfully induced the Portevin–Le Chatelier (P–L) effect and, surprisingly, a distinct fatigue limit when specimen with a small artificial defect was used [6]. Such a discovery (or more mildly termed an *interesting similarity* to ferrous alloys) had never been explicitly reported to the best of authors' knowledge.

Although the novelty and importance of the above phenomenon have been rapidly indicated in the previous short note [6], the contents of the investigation remained rather introductory; it lacked e.g. the detailed information on the strain-aging property (strain rate/temperature dependency), the critical comparison of the growth property of life-controlling small crack during coaxing effect test, the quantification of fatigue crack growth (FCG) resistance in terms of the fracture mechanics, etc. In addition, the compositional design of the first prototype alloy, which was not necessarily optimized for thermal processing, had to be further modified for practical use.

In this paper, the authors fully supplement the previously unaddressed data and revisit the characteristic mechanical and HCF properties of the newly developed Al alloy in detail. Note that these evaluations are thoroughly conducted again by using the modified version of the new Al alloy (second prototype), which will provide not only a demonstration to the previous studies but also a reliable basis for the forthcoming studies.

2. Materials and methods

The chemical composition of the tested Al alloys is listed in Table 1. The new alloys contain ca. 0.5wt% and 0.8wt% extra Mg compared with the base alloy with a stoichiometric Mg_2Si composition (Mg : Si = 1.73 : 1, mass ratio). The thermal process for the alloys is schematically shown in Fig. 1. The homogenized ingots were pre-heated at 723 K (450 °C) and die-extruded to form a round bar (ϕ23 mm) at a velocity of 50 mm s^{-1}. During the extrusion process, the alloys were self-heated and eventually solutionized at ca. 773 K (500 °C). The base alloy was then immediately water-quenched. The new alloys, on the other hand, had to go through another solution treatment at a higher temperature of 813 K × 3.6 ks (540 °C × 1 h) because the solubility of Mg_2Si in the new alloys was significantly reduced by the extra Mg when compared with the base alloy [13-15]. This inevitably caused extreme grain coarsening (recrystallization) particularly at surface region where severe flow strain was imposed during die extrusion (see Fig. 2) [16]. Such a side effect, which eventually caused significant material loss in the previous prototype, was prevented by adding ca. 0.15% zirconium (Zr) to the alloys; the addition of Zr or scandium (Sc) has been shown to remarkably restrict grain coarsening by pinning grain boundaries [17-19]. After quenching, all alloys were age-hardened (463 K× 14.4 ks; 190 °C × 4 h) to obtain the peak hardness. The typical microstructure of the alloys is shown in Fig. 3. The grains in all alloys are either {111} or {100} oriented along the extrusion direction; see (a) and (b). The needle-like β" precipitates (G.P. zone) oriented along the <100> are seen in both alloys; see (c). The precipitates aligned parallel to the electron beam direction (i.e. normal to the printed surface) are shown as dots. The precipitates in the new alloy are generally finer and denser than those in the base alloy. Other information regarding grain size, hardness (both of which was measured on the cross-sectional plane normal to the extrusion direction) and 0.2% proof strength are listed in Table 2. Note that the grain size of the new alloy is somewhat larger than the base alloy owing possibly to the higher solutionization temperature. This is, however, tolerable as it has no negative effect on the resultant hardness and strength after

aging treatment.

Specimens for tensile tests and fatigue tests were prepared from the above alloys. Fig. 4 shows specimen geometry. For tensile tests, dog-bone shaped specimens having gauge length and diameter of 30 mm and 8 mm, respectively, were machined parallel to the extrusion direction. For fatigue tests, gauge length and diameter of 20 mm and 5 mm, respectively, were machined parallel to the extrusion direction. The gauge portion of the fatigue specimens was electropolished to remove damaged surface layer, and a small blind hole (diameter/depth: 300 μm/300 μm) was drilled at the center of the gauge portion as a crack starter.

Tensile tests were conducted by using a uniaxial tester (AG-Xplus^{TM}, Shimadzu Ltd.) whose load capacity was 50 kN. The gauge displacement was measures with a digital video type extensometer (TRView X^{TM}, Shimadzu Ltd.). The effects of strain rate and temperature on deformation properties were evaluated: strain rate was changed by three orders of magnitude ($5.6 \times 10^{-5} \sim 5.6 \times 10^{-3}$ s^{-1}) under the same temperature (298 K; 25 °C), and three different temperatures (298, 323 and 373 K; 25, 50 and 100 °C) were employed and controlled within ± 3 K (°C) during the tests (strain rate: 5.6×10^{-4} s^{-1}). All the tests were conducted in ambient air.

Fatigue tests were conducted by using a multiple rotating bending tester (GIGA QUAD^{TM} YRB200, Yamamoto Metal Technos Co. Ltd.) that allowed four parallel testing at the same time. The machine employed cantilever bending as the loading method; one end of the specimen was fixed to the spindle by a collet chuck, and the other end was loaded by a dead weight. Since this loading mode inherently generated small amount of shear stress which was completely absent in pure bending mode (e.g. Ono-type tester), the fatigue properties of 6061-T6 alloy were preliminarily compared in these different methods. No differences regarding fatigue crack growth (FCG) property and the resultant fatigue life were confirmed. The comparison of the present study to the former ones [6,7] using Ono-type tester is therefore acceptable. All the tests were conducted in ambient air at room temperature, fatigue frequency and stress ratio of 50 Hz and -1, respectively. FCG was mainly

observed by plastic replica technique, and supplement analyses were also done by the scanning electron microscopy (SEM).

3. Results

3.1 Tensile properties

Fig. 5 shows the stress-strain behavior of three alloys (base, 0.5%Mg added, 0.8%Mg added) under different strain rate conditions. In the uniform deformation stage before ultimate tensile strength (UTS) is achieved, no eminent strain rate effect is observed in the base alloy within the current range. On the other hand, the new alloys clearly show strain rate dependency; the flow stress generally becomes higher at lower strain rate. Such negative strain-rate-sensitivity (nSRS) is seen to be also accompanied by serrated flow (P–L effect) [20-22] which is eminent at lower strain rate and at higher Mg content. Note that a normal 6061-T6 alloy, like other pure metals, has been reported to show positive strain-rate-sensitivity (pSRS), while its rate dependency to be very weak at strain rate less than 10^{-1} s^{-1} [23]. Hence the observed nSRS in the new alloys at the current strain rate range ($\ll 10^{-1}$ s^{-1}) is rather a unique characteristic.

Fig. 6 shows the effect of temperature on stress-strain behavior. The constant decrease of flow stress at higher temperature is eminent in the base alloy; UTS decreases 40 MPa at 373 K. The new alloys, on the other hand, are much more insensitive to temperature rise; flow behavior is almost the same between R.T. and 323 K (or even slightly higher at 323 K), and the decrease of UTS at 373 K is 20 MPa and 12 MPa for 0.5%Mg alloy and 0.8%Mg alloy, respectively. The weak (or partly inverse!) temperature sensitivity is quite noteworthy as it suggests that the present new alloys have potential benefit in high-temperature usage that the conventional 6061-T6 has not been applied.

Fig. 7 shows the relation between work-hardening rate, $d\sigma/d\varepsilon$, and flow stress, σ, at different strain rates. The data shown here were taken from smooth σ–ε curves fitted to the original serrated curves. The work-hardening rate of the new alloys is clearly higher than that of the base alloy

particularly at lower strain rate, and the difference of work-hardening behavior due to different Mg content (0.5%, 0.8%) is not so large in the current comparison. The pronounced work-hardening behavior of the new alloys is reminiscent of that typically observed in solute-hardened Al-Mg alloys [20,21,24,25] that also exhibit P–L effect. The clear effect of strain rate shown here again suggests the strain-aging characteristic (i.e. *the slower the stronger*) of the new alloys.

3.2 Fatigue test

3.2.1 S-N behavior analysis

Fig. 8 shows the *S-N* diagrams of the base alloy and the new alloy (0.5%Mg added). The overall fatigue strength of the new alloy is superior to the base alloy. Such a difference at finite life regime is primarily attributed to the different FCG resistance as shown in Fig. 9; the FCG in the new alloy is generally slower than the base alloy. The evolution of crack shape is schematically shown in the figure: two corner cracks are independently initiated at the hole brim where the elastic stress concentration is maximum (step (i)); the two cracks are connected behind the hole and form a thumbnail crack (step (ii): $l \approx 500$ μm); the thumbnail crack keeps the similar shape and continues growing (step (iii): $l > 500$ μm). The aspect ratio (a/c) of the thumbnail cracks in steps (ii) and (iii) was confirmed by statically fracturing the pre-fatigued specimens; $a/c = 0.86$ was obtained. Then, a semi-circular assumption ($a/c = 1$) was employed and the stress intensity factor range (ΔK) at the deepest point ($\phi = \pi/2$) was calculated with the following formula for a semi-circular surface crack in a semi-infinite body under mode I loading [26]:

$$\Delta K = \frac{2.2}{\pi} \sigma_a \sqrt{\pi l / 2} \qquad (1)$$

The FCG resistance represented by dl/dN-ΔK relation is shown in Fig. 10. It can be seen that the new alloy exhibits higher resistance particularly at high ΔK regime. It should be added that the data shown in Fig. 10 may not be regarded as that of a long crack measured with a standard fracture

mechanics specimen because the present crack dimension is less than a few millimeters [4].

The *S-N* diagram of the base alloy can be approximated to a smooth continuous curve; N_f gradually increases with decreasing σ_a even beyond 10^6-cycle-orders. Note that such a trend is the same as that observed for unalloyed pure Al [27-30] or 6061 with higher Si content [2]. In contrast, the curve of the new alloy shows clear discontinuity; N_f significantly increases at σ_a between 90 MPa and 95 MPa (fatigue limit: 92.5 MPa). Fig. 11 shows the FCG behavior of a run-out specimen of the new alloy fatigued slightly below the fatigue limit ($\sigma_a = 90$ MPa, 1.0×10^8 cycles). It is seen that the initiated cracks (denoted as C1 and C2) gradually decelerate to the growth rate order of 10^{-13} m cycle^{-1}, which can be regarded as almost non-propagating. Such non-propagating cracks were also seen in other run-out specimens. The distinct fatigue limit of the new alloy can therefore be viewed as the threshold against small crack growth.

3.2.2 Coaxing effect analysis

Base alloy

Fig. 12 and Table 3 summarize the results of σ_a step-up tests for the base alloy. Three specimens (Nos. B1, B2 and B3) were pre-fatigued to certain cycles at relatively low σ_a, and the subsequent σ_a was gradually increased ($\Delta\sigma_a = 2.5$ MPa) when the specimen passed 10^7 cycles without failure. In the cases of specimens B1 and B2, no life-controlling cracks appeared before the final σ_a step; N_f values of B1 and B2 were determined by the cracks emanated at the final σ_a steps of 85 MPa and 87.5 MPa (not shown in the figure), respectively. As the N_f values of B1 and B2 at the final step are comparable to that of virgin ones (see Fig. 12(a)), the fatigue history before the final step has no influence in these specimens. In the case of specimen B3, on the other hand, a non-propagating crack (M1) appeared during the pre-fatigue period ($\sigma_a = 75$ MPa, 1.5×10^8 cycles). This micro crack showed no eminent growth even after the fourth $\Delta\sigma_a$ was completed (see Figs. 12(b)(c)). Another micro crack (M2), which was absent in the pre-fatigue period, appeared during the σ_a step-ups

although its growth rate was significantly slow (ca. 10^{-14} m cycle^{-1}). As the dimension of these cracks

is several times the grain size, they can be considered as microstructurally small cracks whose

growth is hindered e.g. by a large inclusion or a grain boundary with a relatively large orientation

difference [2,31-33]. The σ_a step-ups in specimen B3 can then be interpreted as an extra driving

force required for overcoming the incidentally imposed microstructural barriers. In summary of

these results, it is postulated that the base alloy exhibits no eminent *coaxing effect* (i.e. intrinsic

strengthening) where the specimen is "coaxed" to attain a better fatigue resistance during the gradual

σ_a step-ups [8].

New alloy

Fig. 13 and Table 3 summarize the results of σ_a step-up tests for the new alloy (0.5%Mg added).

Three specimens (Nos. N1, N2 and N3) were pre-fatigued to 1×10^8 cycles at σ_a lower than the

fatigue limit, and infinitesimal $\Delta\sigma_a$ (= 2.5 MPa) was applied every 10^7 cycles except for N3 (every

10^6 cycles). The FCG behavior in specimen N1 is particularly focused here. A few small cracks, one

of which became the life-controller (M1) in the later stage, had already appeared in the pre-fatigue

cycles (σ_a = 85 MPa, ~ 1.0×10^8 cycles) as shown in Figs. 13(b)(c). The application of $\Delta\sigma_a$ further

promoted initiation of other small cracks including the second life-controller (M2). At this point,

these cracks were confirmed to be independent of each other by SEM. M1 and M2 then continued to

grow exclusively and completely coupled behind the drill hole when σ_a = 107.5 MPa was passed

(see Fig. 13(c)) although the growth rate during the σ_a step-ups was generally very small (< 10^{-12} m

cycle^{-1} order). The united cracks eventually bore the 10th $\Delta\sigma_a$ without shifting to a fatal growth

mode. The maximum ΔK achieved by this *quasi*-non-propagating crack at the semifinal step (σ_a =

110 MPa, 1.0×10^7 cycles) is calculated by Eq. (1) as 2.6 MPam$^{1/2}$, which would normally cause

orders of magnitude faster FCG in a specimen with no pre-fatigue treatment (see Fig. 10). The N_f

value at the final step (σ_a = 112.5 MPa) is also far larger than that of the normally fatigued sample.

The FCG in specimen N2 showed the same trend as N1. All these data clearly suggest the presence of coaxing effect in specimens N1 and N2.

It is interesting to note that specimen N3, whose fatigue cycles in each step was ceased at much short cycles (10^6 cycles), shows no sign of coaxing effect; N_f of N3 at the final step (σ_a = 112.5 MPa) is almost the same as the normally fatigued sample. In other words, the manifestation of coaxing effect is dependent on the duration of each σ_a step.

4. Discussion

Originally, the modification of the stoichiometric 6061 alloy composition with extra Si or Mg has been an important issue from a plasticity processing viewpoint [14-15]; these extra elements have been shown to affect various indices such as proof strength, UTS, ductility (formability) [16]. The addition of excess Si has now become an important measure to improve these indices except that it generally reduces toughness and hence formability [14,16,34]. The effect of extra Mg, on the other hand, has not been extensively (and perhaps *eagerly*) investigated as that of Si owing possibly to its overriding negative impact (i.e. significant lowering of Mg_2Si solubility and the resultant insufficient strengthening). Meanwhile, the present study shows that such a negative effect of adding Mg can be effectively avoided by combining appropriate thermal process condition and compositional design: the strength level at initial flow (proof strength) is maintained and, moreover, the subsequent work-hardenability (plus strain-aging capability) is further introduced. Such characteristics are attributed to the coexistence of G.P. zone (for Al-Mg_2Si quasi-binary alloy, Mg : Si = 2 : 1, atomic ratio [35]) and the unbound Mg atoms that remain as free solutes.

It is well known that the emergence of P–L effect (one of the manifestation of strain-aging capability) and its properties in Al-Mg binary alloys depend on temperature, strain rate and Mg content as has been extensively investigated e.g. by Král and Lukáč (Al-2.75%Mg, Al-4.8%Mg) [36] or by Pink and Grinberg (Al-5%Mg) [37]. The amount of Mg in these examples is, however,

relatively higher than the present study (< 1.0%), which restricts a quantitative comparison. Table 4 summarizes the conditions where P–L effect is observed in alloys containing dilute Mg (< 1%). Note that the table includes data obtained for as-quenched (unaged) or annealed (O-tempered) Al-Mg$_2$Si alloys containing Mg as free solutes. It can be seen that the P–L sensitivity of the present new alloy on each parameter is by and large the same as these reported cases. This may again suggests that the coexistence of G.P. zone in the matrix have little effect on the strain-aging capability of the present new alloy.

The drastic change of HCF properties by the addition of extra Mg is clearly demonstrated; the *S-N* diagram of the present new alloy (i.e. the second prototype material) exhibits a distinct knee-point in 10^6-cycle-order which is absent in the base alloy (Fig. 8). Such a sudden jump of fatigue life is obviously attributed to the arrest of a small crack which would lead the specimen to failure at a slightly higher σ_a level. The self-arrest of a small crack under constant σ_a level is, however, a phenomenon also incidentally found in the base alloy (Fig. 12). The existence/inexistence of a distinct threshold against small FCG (as well as the coaxing effect) in these different alloys should then be discussed in terms of the different underlying micro-mechanisms.

Several mechanisms can account for the self-arrest of small fatigue cracks in general: they are typically (i) grain/phase boundary blocking of the crack tip slip [31-33], (ii) crack closure effect [4,42] and (iii) local work hardening around the crack tip [43]. Since (i) is essentially a stochastic factor that can be expected in both alloys, it is difficult to rationally explain the distinct threshold that appeared only in the new alloy. The factor (ii), which is an extrinsic type of resistance that reduces the true driving force (ΔK_{eff}), is expected to play a certain role in retarding FCG. It is, however, difficult to explain the clear coaxing effect that appeared only in the new alloy. It then appears that the factor (iii) plays an important role in the characteristic small crack behavior in the new alloy.

Note that the effect of notch-induced K transient [44] is believed to be not important in the present

case: this mechanism is said to count only when the crack length from the notch root falls in the range of $r/20 \sim r/4$ (r: notch radius) if an ordinary elliptical notch with $k_t > 2$ (k_t: stress concentration factor) is of concern. Another type of notch effect that results from the notch-tip plasticity (i.e. the temporal retardation or arrest of a small crack embedded in the notch-tip plastic zone [4]) can be neglected in the present case: the local σ_a at the hole brim ($k_t\sigma_a$), at which non-propagating cracks were observed, is calculated to be $190 \sim 230$ MPa ($k_t = 2.5$ [45]), which is much smaller than the proof stress (> 300 MPa).

It should be recalled that the enhancement of work-hardening in the present new alloy can be attributed to its strong strain-aging capability (i.e. *time-dependent* strengthening mechanism). In addition, the new alloy shows much higher work-hardenability than the base alloy particularly at the initial flow regime (see Fig. 7). It is therefore postulated that the resistance against cyclic slip at the initial crack tip is significantly increased by the factor (iii) to the extent that it hardly continue at the applied ΔK level. In this first retardation process, crack tip slip may be also shifted to a non-localized mode by Mg solutes and perhaps facilitate crack closure. Once the FCG is retarded, the crack tip resistance can be further increased by solute aging provided that the constant σ_a level is prolonged for a long time period (e.g. > 10^7 cycles). Such a time-dependent strengthening mechanism successfully keeps the FCG almost negligible even though the applied σ_a is slightly shifted to a higher level. The solute stabilization effect keeps the life-controlling crack to be quasi-non-propagating until the applied ΔK finally overrides the effect and a usual fast FCG mode is attained. On the other hand, the solute stabilization effect cannot be expected in the base alloy as no extra solute Mg is present in the matrix. It is also noted that the base alloy is susceptible to slip localization caused by the shearing of precipitates [46,47]. These factors are believed to concurrently cause significant slip instability: the crack tip slip process is likely to continue even though it is temporarily shielded e.g. by grain boundaries [2]. This is why the base alloy exhibits neither a distinct threshold in its *S-N* curve nor a clear coaxing effect.

Although the emergence of a distinct fatigue limit in the new age-hardened Al alloy is an eye-opening phenomenon, it has been only observed in specimens with a surface blind hole. Our previous survey on electropolished smooth specimens (0.5%Mg added, first prototype alloy) confirmed no distinct fatigue limit [7], indicating that the mechanical threshold for the initiation and/or propagation of the life-controlling cracks was not uniquely dependent on the nominal σ_a value. Such a property was attributed in part to the different crack initiation life that strongly depended on the microscopic inhomogeneity (e.g. stress concentration at intermetallic particles of different size, differently oriented slip planes, different grain size, etc.). The complexity could also arise from the competition of multiply initiated cracks [48]: even though one crack was arrested (and strain-aged), other larger cracks that incidentally attained much higher ΔK eventually determined the fatigue life. Note, however, that such an interpretation seem to be only viable for the present case and not applicable to the nominally defect-free steel specimens that exhibit distinct knee [8-10,43,49].

Apart from the effect of specimen geometry, the present new alloy may exhibit characteristic HCF properties depending on loading frequency or temperature, both of which are important factors from the viewpoint of strain-aging. These issues will be addressed elsewhere.

4. Conclusions

The main results obtained in this study are summarized as follows.

(1) A new 6XXX type age-hardened Al alloy was developed by adding small amount of Mg (0.5%, 0.8%) to the normal 6061-T6 alloy with a stoichiometric Mg_2Si composition. By adding ca. 0.15% Zr to the new alloy, significant grain coarsening during thermal process was effectively restricted.

(2) The tensile flow stress of the new alloy exhibited negative strain-rate sensitivity (nSRS) which was absent in the normal base alloy.

(3) The tensile flow stress of the new alloy was relatively insensitive to temperature rise when

compared with the normal base alloy.

(4) The work-hardening rate of the new alloy is much higher than the base alloy particularly at the initial flow regime and at low strain rate.

(5) The *S-N* diagram of the new alloy (0.5%Mg added) showed distinct fatigue limit (92.5 MPa) which was determined as the threshold against propagation of small cracks. The base alloy, on the other hand, showed no distinct knee-point.

(6) The new alloy exhibited a clear coaxing effect which was absent in the base alloy. The coaxing effect was controlled by the existence of a small quasi-non-propagating crack whose growth resistance gradually increased before shifting to the fatal FCG mode.

References

[1] F. King, Aluminium and its Alloys, Ellis Horwood, Chichester, 1987.

[2] Y. Takahashi, T. Shikama, S. Yoshihara, T. Aiura, H. Noguchi, Acta Mater. 60 (2010) 2554–2567.

[3] Fatigue Data Book: Light Structural Alloys, ASM International, Materials Park, 1995.

[4] S. Suresh, Fatigue of Materials. second ed., Cambridge University Press, Cambridge, 1998.

[5] D.G. Altenpohl, Aluminum: Technology, Applications, and Environment, A Profile of a Modern Metal, sixth ed., TMS, Warrendale, 1998.

[6] T. Shikama, Y. Takahashi, L. Zeng, S. Yoshihara, T. Aiura, K. Higashida, H. Noguchi, Scr. Mater. 67 (2012) 49–52.

[7] L. Zeng, T. Shikama, Y. Takahashi, S. Yoshihara, T. Aiura, H. Noguchi, Int. J. Fatigue 44 (2012)

32–40.

[8] G.M. Sinclair, ASTM Proc. 52 (1952) 743–758.

[9] G. Oates, D.V. Wilson, Acta Metall. 12 (1964) 21–33.

[10] B. Mintz, D.V. Wilson, Acta Metall. 13 (1965) 947–956.

[11] H.A. Lipsitt, D.Y. Wang, Trans. AIME 221 (1961) 918–923.

[12] M. Hansen, K. Anderko, Constitution of Binary Alloys, second ed., McGraw-Hill, New York, 1958.

[13] H.W.L. Phillips, Annotated Equilibrium Diagrams of Some Aluminium Alloy Systems, Inst. of Metals, London, 1959.

[14] R.C. Dorward, C. Bouvier, Mater. Sci. Eng. A254 (1998) 33–44.

[15] J. Langerweger, Proc. Int. Conf. on Aluminium Technology, 1986, pp. 216–222.

[16] I.J. Polmear, Light Alloys from Traditional Alloys to Nanocrystals, fourth ed., Butterworth-Heinemann, Oxford, 2006.

[17] J.X. Li, T. Zhai, M.D. Garratt, G.H. Bray, Metall. Trans. 36A (2005) 2529–2539.

[18] N. Blake, M.A. Hopkins, J. Mater. Sci. 20 (1985) 2061–2867.

[19] Z. Yin, Q. Pan, Y. Zhang, F. Jiang, Mater. Sci. Eng. A280 (2000) 151–155.

[20] J.G. Morris, Mater. Sci. Eng. 13 (1974) 101–108.

[21] D. J. Lloyd, Metall. Trans. 11A (1980) 1287–1294.

[22] S. Zhao, C. Meng, F. Mao, W. Hu, G. Gottstein, Acta Mater. 76 (2014) 54–67.

[23] K. Ogawa, JSME Int. J. Ser. A, 46 (2003) 322–327.

[24] M. Verdier, M. Janecek, Y. Bréchet, P. Guyot, Mater. Sci. Eng. A248 (1998) 187–197.

[25] D. J. Lloyd, Metall. Trans. 13A (1982) 1445–1452.

[26] G.R. Irwin, J. Appl. Mech. 29 (1962) 651–654.

[27] T. Tanaka, H. Nakayama, Bull. JSME, 18(1975) 1365-1374.

[28] S.Y. Zamrik, L.W. Hu, Exp. Mech. 5 (1967) 193–201.

[29] S. Kobayashi, T. Inomata, H. Kobayashi, S. Tsurekawa, T. Watanabe, J. Mater. Sci. 43 (2008) 3792–3799.

[30] F. Djavanroodi, M. Ebrahimi, B. Rajabifar, S. Akramizadeh, Mater. Sci. Eng. A528 (2010) 745–750.

[31] K. Tanaka, Y. Akiniwa, Y. Nakai, R.P. Wei, Eng. Fract. Mech. 24 (1986) 803–819.

[32] Y.H. Zhang, L. Edwards, Scr. Mater. 26 (1992) 1901–1906.

[33] H. Toda, T. Kobayashi, Metall. Mater. Trans. 27A (1996) 2013–2021.

[34] S.M. Hirth, G.J. Marshall, S.A. Court, D.J. Lloyd, Mater. Sci. Eng. A319–321 (2001) 452–456.

[35] M. Murayama, K. Hono, Acta Mater. 47 (1999) 1537–1548.

[36] R. Král, P. Lukáč, Mater. Sci. Eng. A234-236 (1997) 786–789.

[37] E. Pink, A. Grinberg, Acta Metall. 30 (1982) 2153–2160.

[38] S. Zhao, C. Meng, F. Mao, W. Hu, G. Gottstein, Acta Mater. 76 (2014) 54–.

[39] R.B. Schwarz and L.L. Funk, Acta metall. 33 (1985) 295–307.

[40] A. Cuniberti, A. Tolley, M.V. Castro Riglos, R. Giovachini, Mater. Sci. Eng. A527 (2010) 5307–5311.

[41] W.J. Poole, D.J. Lloyd, J.D. Embury, Mater. Sci. Eng. A234-236 (1997) 306–309.

[42] K. Tanaka, JSME Int. J. Ser. A 30 (1987) 1–13.

[43] H. Nisitani, S. Nishida, Bull. JSME 17 (1974) 1–11.

[44] N.E. Dowling, Fatigue Fract. Eng. Mater. Struct. 2 (1979) 129–138.

[45] H. Noguchi, H. Nisitani, H. Goto, JSME Int. J. Ser. 1 32 (1989) 14–22.

[46] H. Gleiter, E. Hornbogen, Mater. Sci. Eng. 2 (1968) 285–302.

[47] E. Hornbogen, K.H. Zum Gahr, Acta Metall. 24 (1976) 581–592.

[48] Y. Takahashi, H. Yoshitake, R. Nakamichi, T. Wada, M. Takuma, T. Shikama, H. Noguchi, Mater. Sci. Eng. A614 (2014) 243–249.

[45] M.Goto, Fatigue Fract. Eng. Mater. Struct. 14 (1991) 833–845.

List of figure captions:

Figure 1   Schematic diagram of heat treatment process.

Figure 2   Cross-sectional view of die-extruded bars: (a) base alloy (as extruded); (b) new alloy after resolutionization (0.5%Mg added, no Zr added); (c) new alloy after resolutionization (0.5%Mg and Zr added). Note that coarse grained outer region is revealed by etching (etchant: 5% sodium hydroxide solution).

Figure 3   Microstructure of base alloy and new alloy (0.5%Mg added): (a) inverse pole figure color maps on cross-sectional planes normal to extrusion direction; (b) {100} pole figure corresponding to the area shown in (a); (c) bright-field TEM images showing G.P. zone (after peak-age treatment). Upper and lower figures for base alloy and new alloy, respectively.

Figure 4   Shape and dimension of specimens (unit in mm): (a) for tensile tests; (b) for fatigue tests.

Figure 5   Effect of strain rate on stress-strain behavior of three alloys (base, 0.5%Mg added, 0.8%Mg added).

Figure 6   Effect of temperature on stress-strain behavior of three alloys (base, 0.5%Mg added, 0.8%Mg added).

Figure 7   Work hardening rate vs. flow stress: effect of strain rate.

Figure 8   Comparison of *S-N* diagrams of base alloy and new alloy (0.5%Mg added). Run-out plots

are indicated with arrows.

Figure 9   Relation between fatigue cycles and apparent crack length in finite life regime: (a) σ_a = 160, 120 MPa; (b) σ_a = 100 MPa. Crack shape at different steps is schematically shown in (c).

Figure 10   Crack growth rate as a function of stress intensity factor range. Both plots are fitted to the Paris' law ($dl/dN = C(\Delta K)^m$). Note that the plots employed here are for cracks longer than 500 μm where semi-circular shape approximation is valid. ΔK value at point A is employed.

Figure 11   Small crack growth behavior in new alloy (0.5%Mg added) fatigued at σ_a = 90 MPa to N = 1.0×10^8 cycles: (a) growth curves of C1 and C2; (b) 60 ° tilted SEM images of C1 and C2. Note that inner crack length ($l_1{}'$ and $l_2{}'$) are corrected to show the actual length measured perpendicular to the wall of the hole.

Figure 12   Results of σ_a step-up tests for base alloy: (a) fatigue history plotted on S-N diagram; (b) growth behavior of life-controlling main cracks (M1, M2) in specimen B3; (c) micrographs of main cracks in specimen B3.
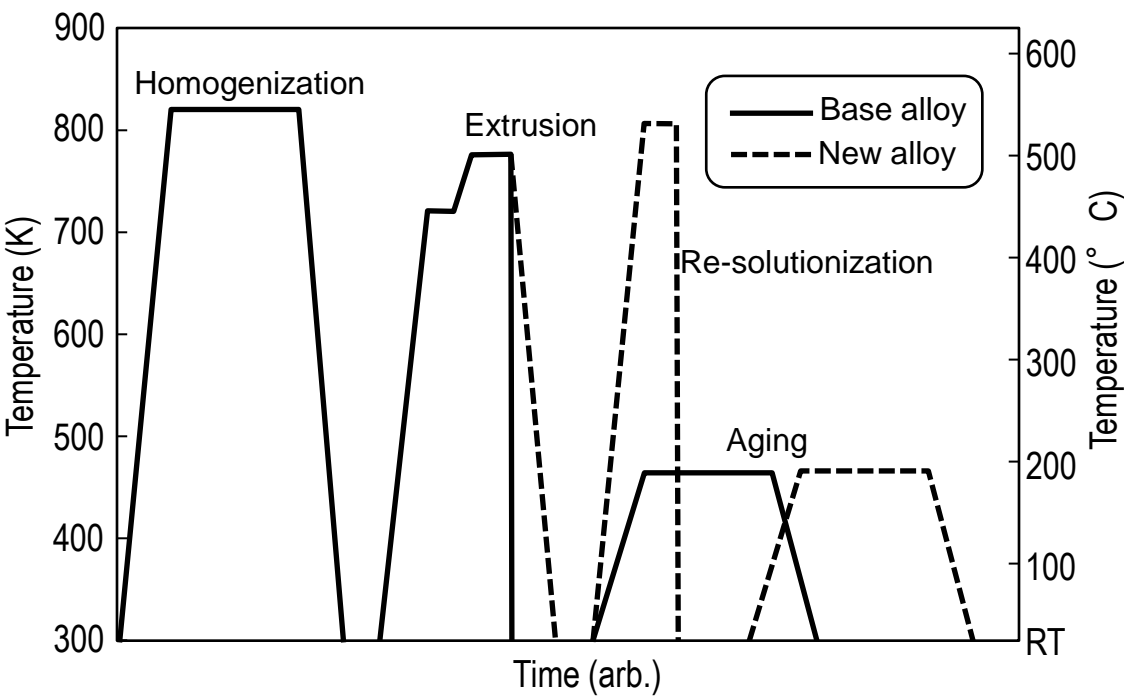
Figure 13   Results of σ_a step-up tests for new alloy (0.5%Mg added): (a) fatigue history plotted on S-N diagram; (b) growth behavior of life-controlling main cracks (M1, M2) in specimen N1; (c) micrographs of main cracks in specimen N1.

fig 1

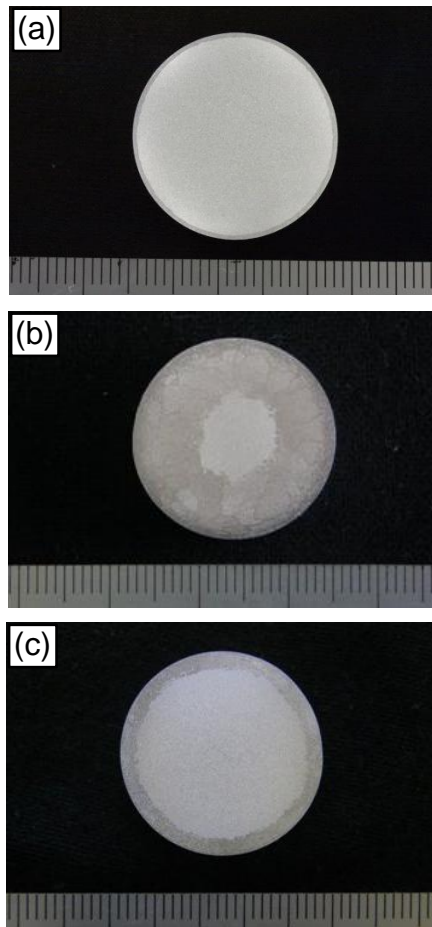Fig. 1. Schematic diagram of heat treatment process.

fig 2

Fig. 2. Cross-sectional view of die-extruded bars: (a) base alloy (as extruded); (b) new alloy after resolutionization (0.5%Mg added, no Zr added); (c) new alloy after resolutionization (0.5%Mg and Zr added). Note that coarse grained outer region is revealed by etching (etchant: 5% sodium hydroxide solution).
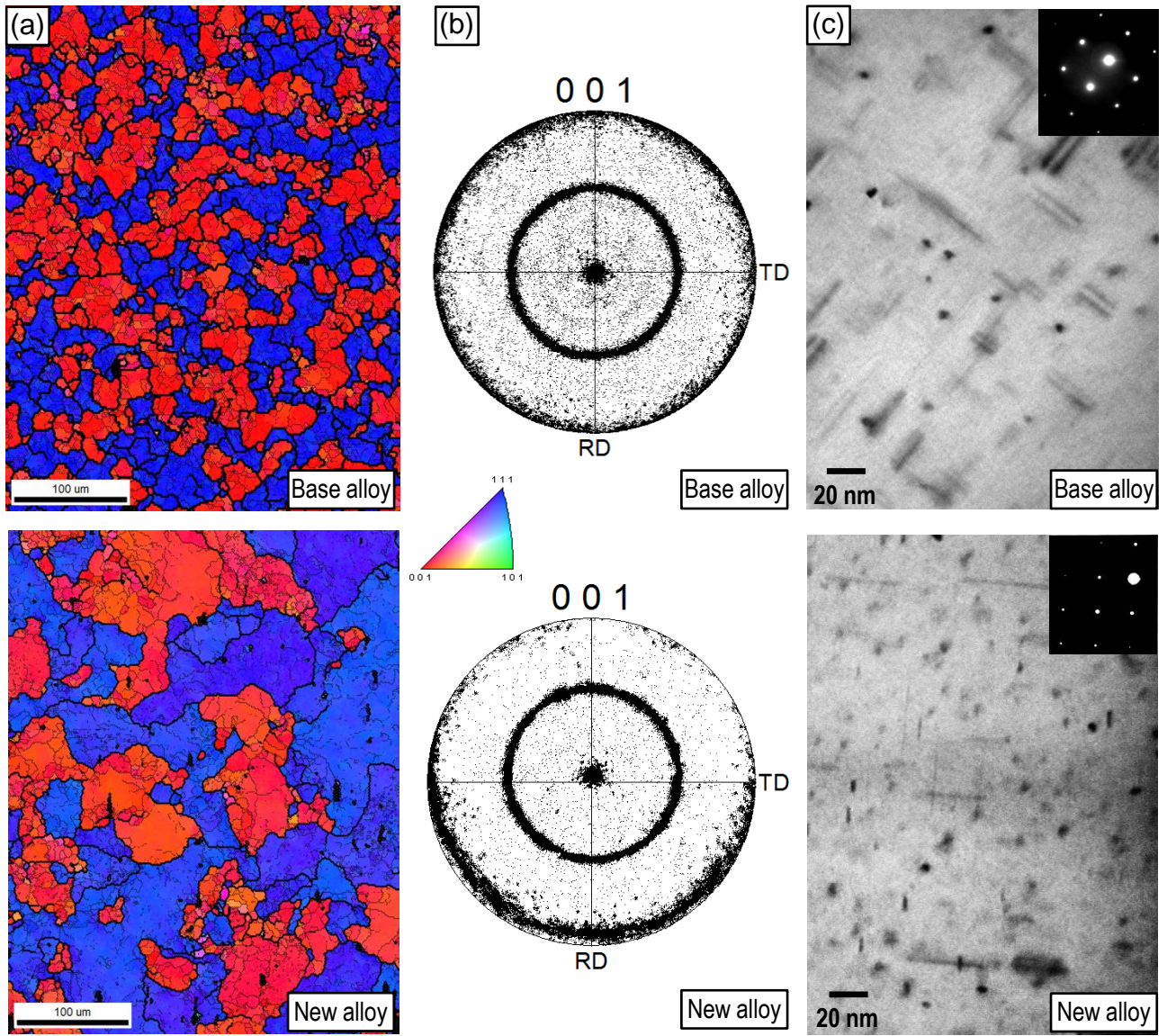
fig 3

Fig. 3. Microstructure of base alloy and new alloy (0.5%Mg added): (a) inverse pole figure color maps on cross-sectional planes normal to extrusion direction; (b) {100} pole figure corresponding to the area shown in (a); (c) bright-field TEM images showing G.P. zone (after peak-age treatment). Upper and lower figures for base alloy and new alloy, respectively.
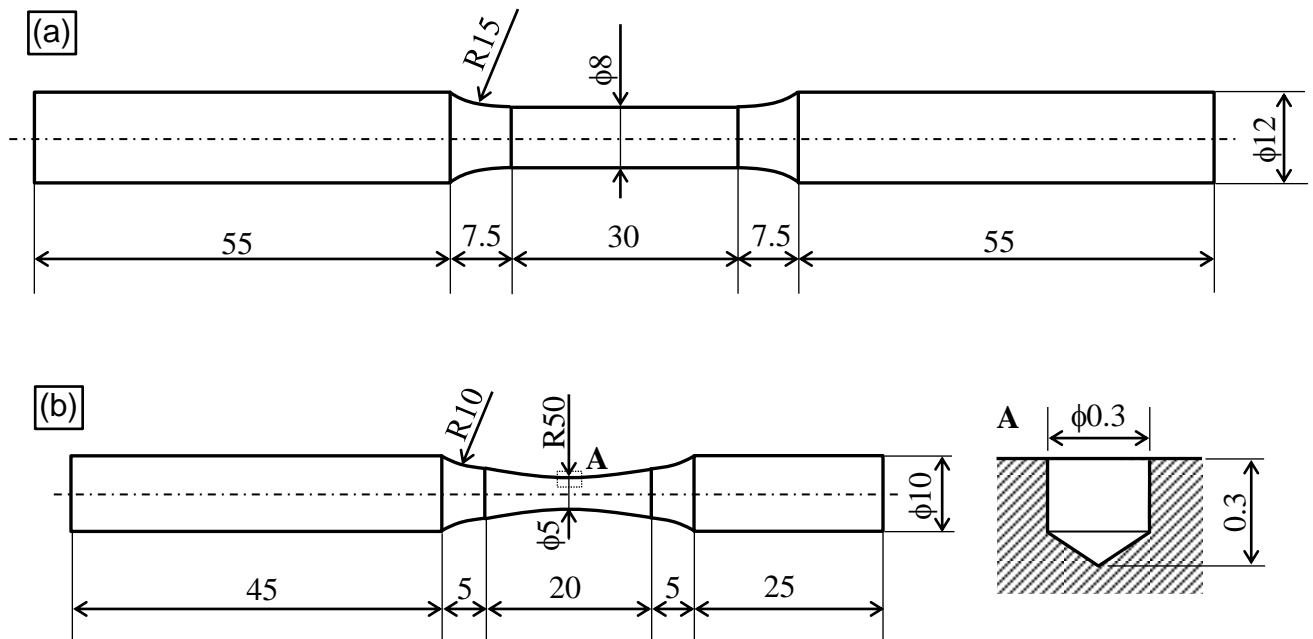
fig 4

(a)

R15 φ8 φ12

55 7.5 30 7.5 55

(b)

R10 R50 A φ5 φ10

A φ0.3 0.3

45 5 20 5 25

Fig. 4. Shape and dimension of specimens (unit in mm): (a) for tensile tests; (b) for fatigue tests.
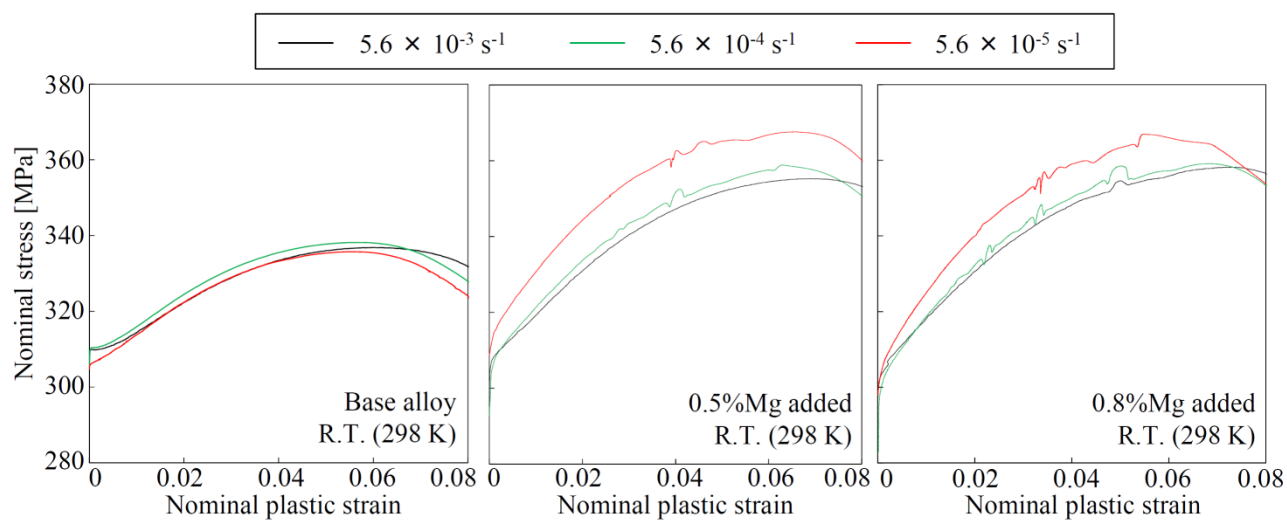
Fig 5

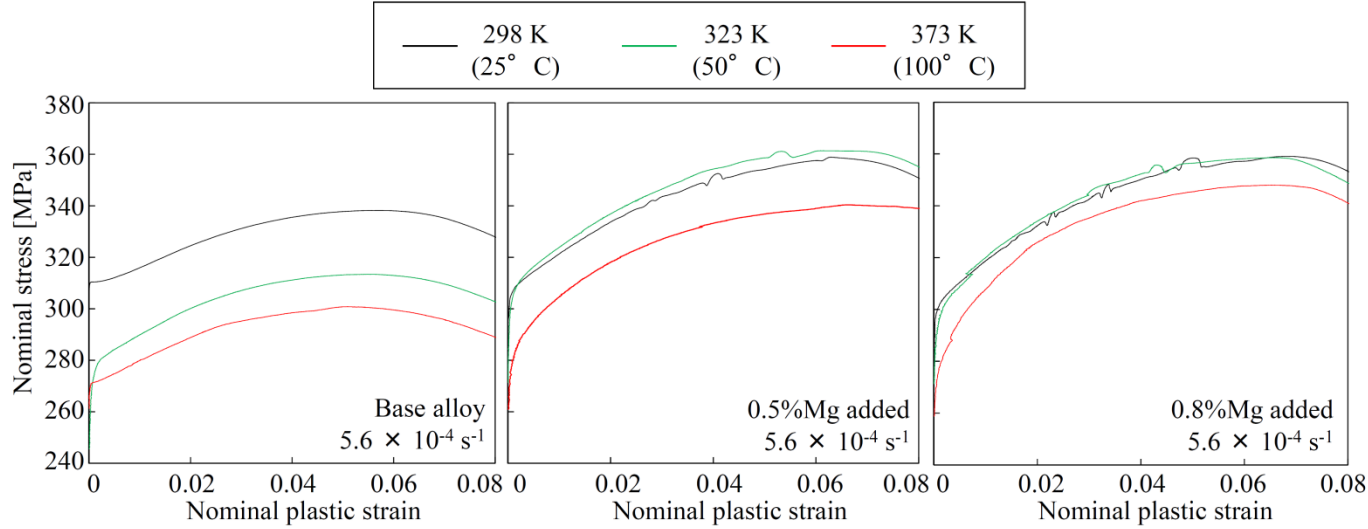Fig. 5. Effect of strain rate on stress-strain behavior of three alloys (base, 0.5%Mg added, 0.8%Mg added).

Fig 6

Fig. 6. Effect of temperature on stress-strain behavior of three alloys (base, 0.5%Mg added, 0.8%Mg added).
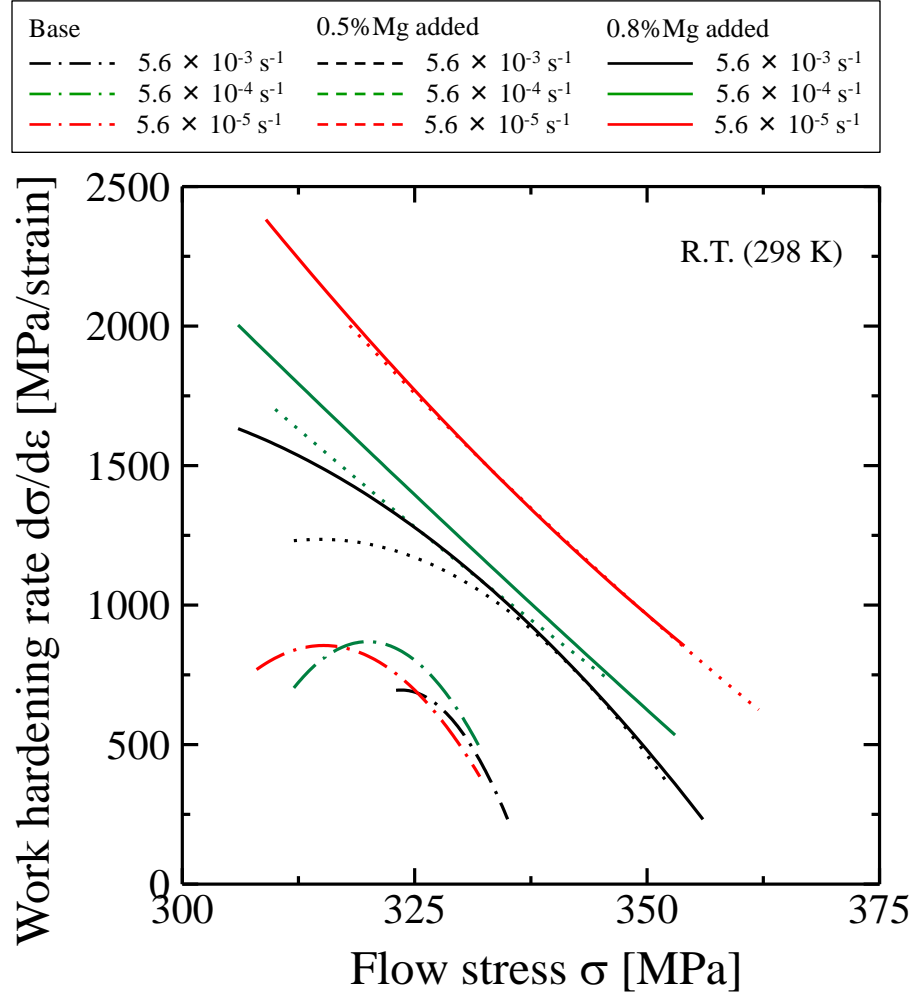
fig 7

Fig. 7. Work hardening rate vs. flow stress: effect of strain rate.
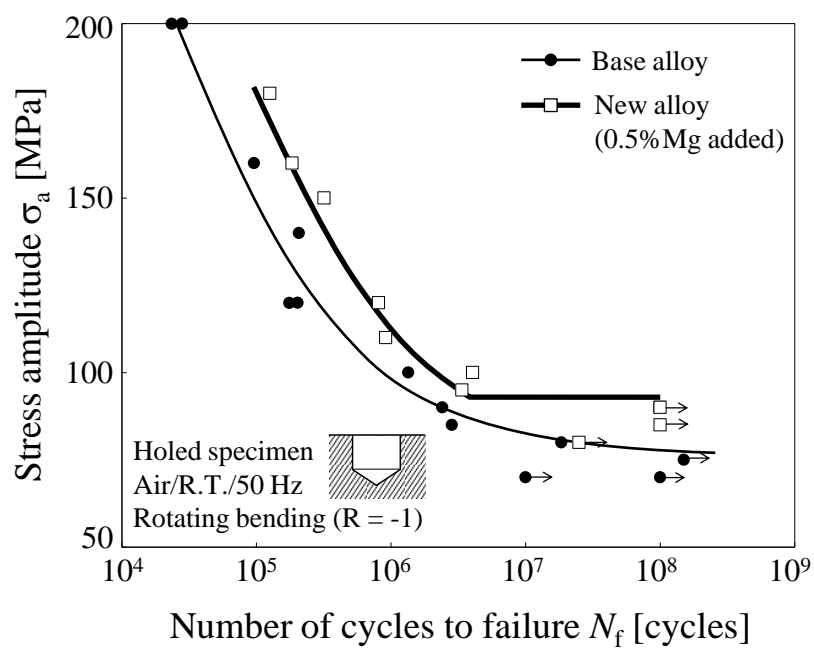
fig 8

Fig. 8. Comparison of *S-N* diagrams of base alloy and new alloy (0.5%Mg added). Run-out plots are indicated with arrows.
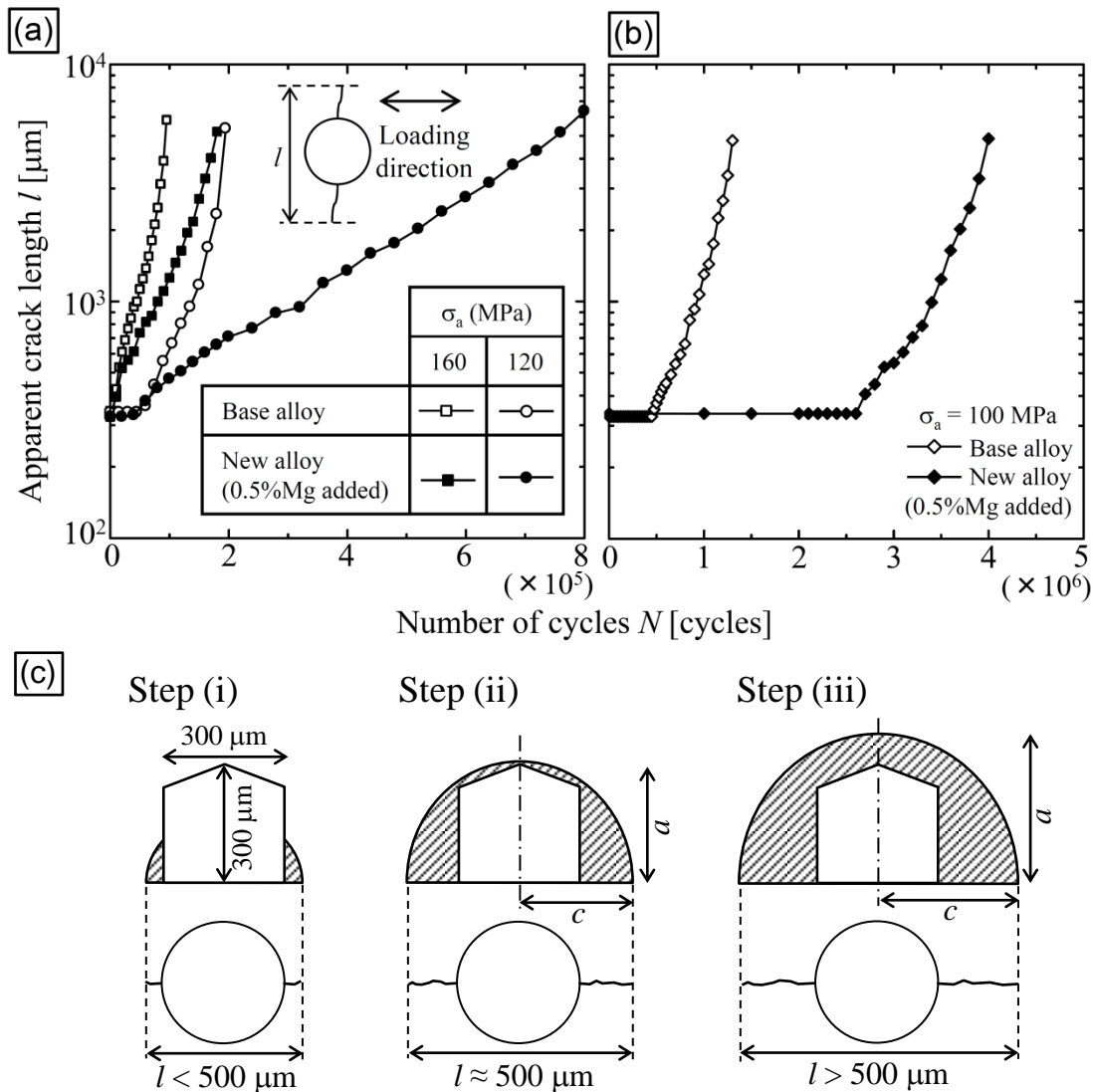
Fig 9

Fig. 9. Relation between fatigue cycles and apparent crack length in finite life regime: (a) σ_a = 160, 120 MPa; (b) σ_a = 100 MPa. Crack shape at different steps is schematically shown in (c).
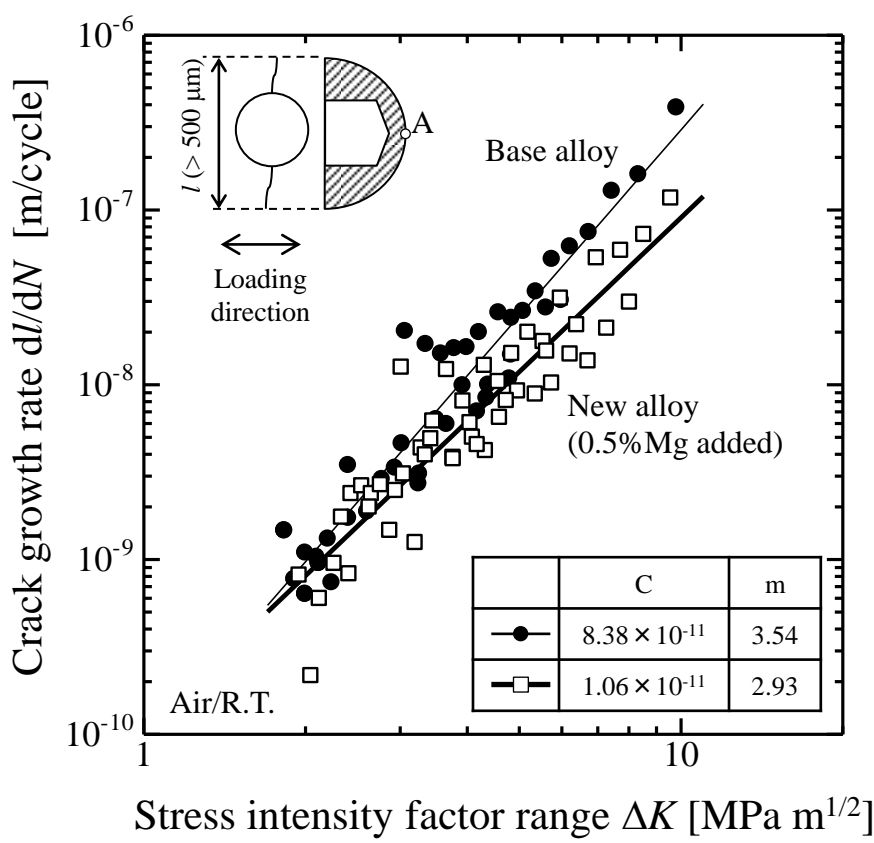
Fig 10

Fig. 10. Crack growth rate as a function of stress intensity factor range. Both plots are fitted to the Paris' law ($dl/dN = C(\Delta K)^m$). Note that the plots employed here are for cracks longer than 500 μm where semi-circular shape approximation is valid. ΔK value at point A is employed.

fig 11
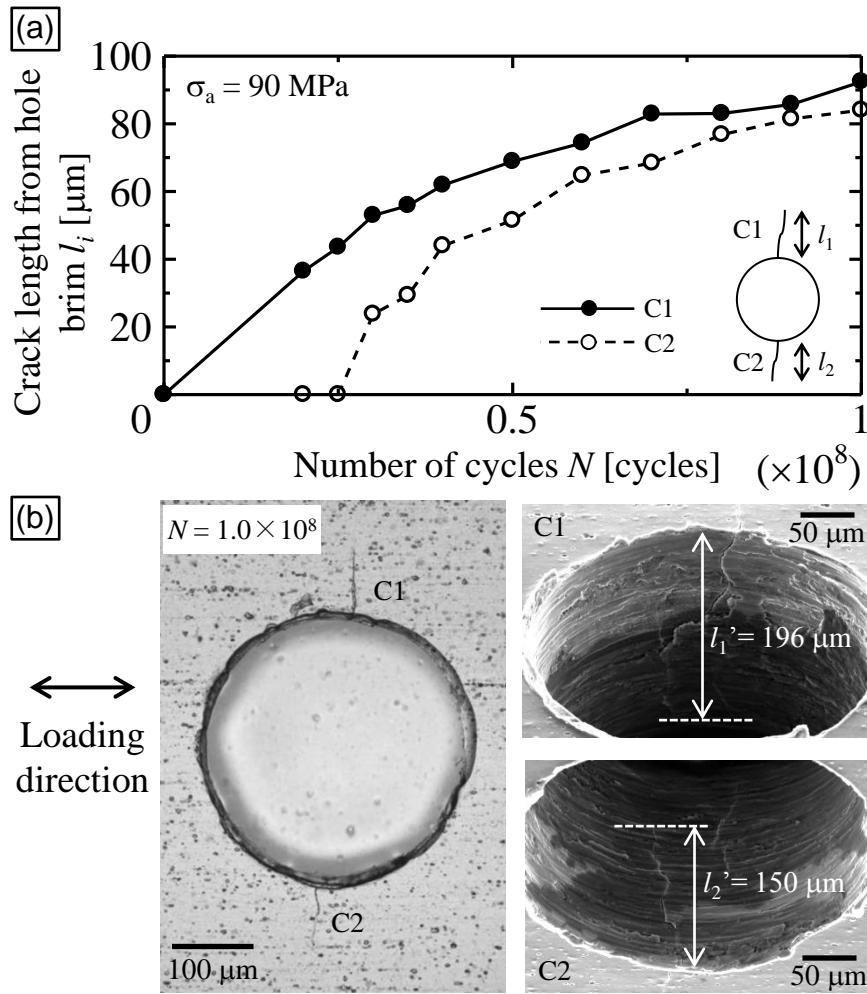

Fig. 11. Small crack growth behavior in new alloy (0.5%Mg added) fatigued at $\sigma_a = 90$ MPa to $N = 1.0 \times 10^8$ cycles: (a) growth curves of C1 and C2; (b) 60° tilted SEM images of C1 and C2. Note that inner crack length (l_1' and l_2') are corrected to show the actual length measured perpendicular to the wall of the hole.

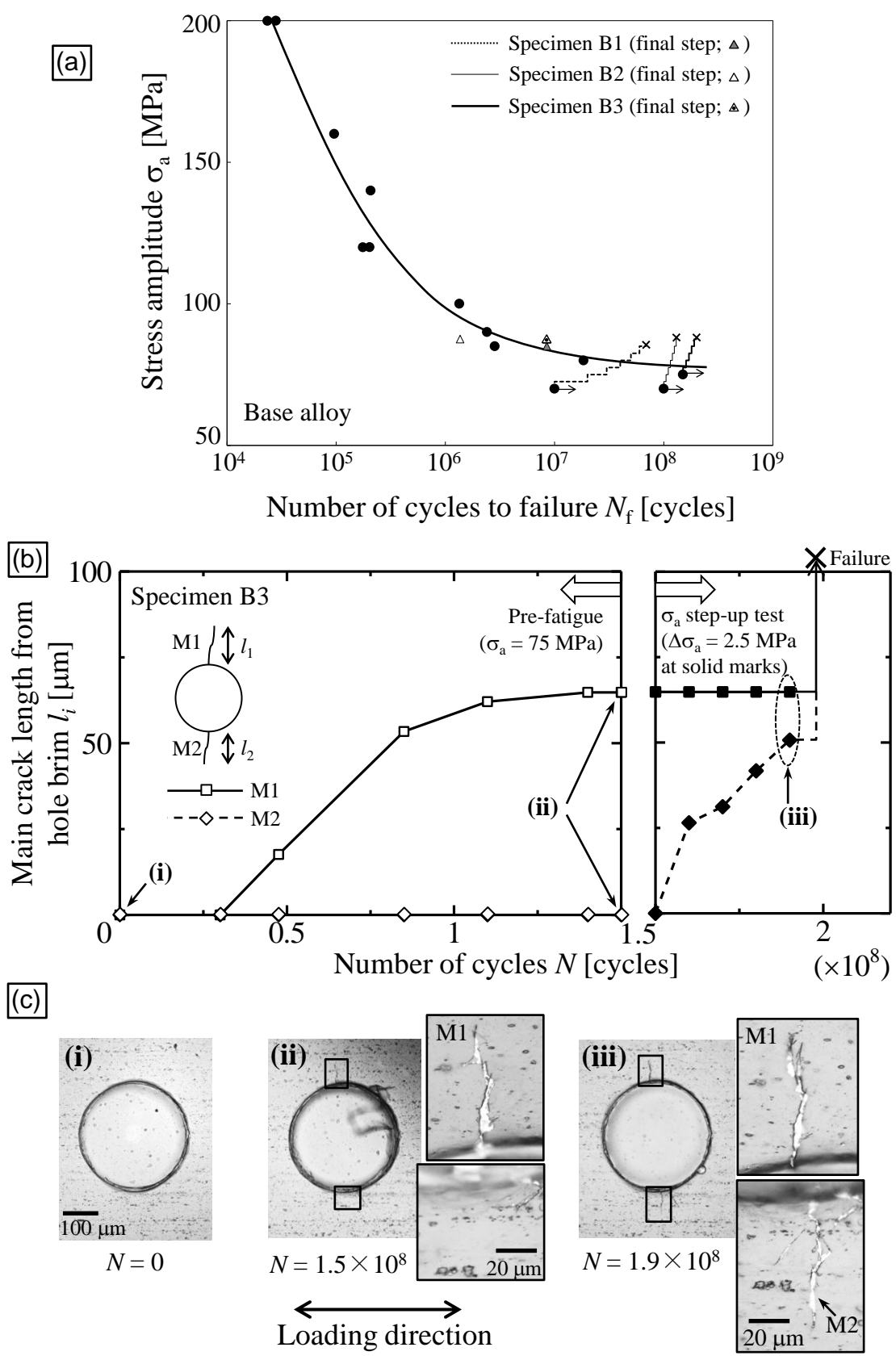**Fig 12**

Fig. 12. Results of σ_a step-up tests for base alloy: (a) fatigue history plotted on *S-N* diagram; (b) growth behavior of life-controlling main cracks (M1, M2) in specimen B3; (c) micrographs of main cracks in specimen B3.

Fig 13

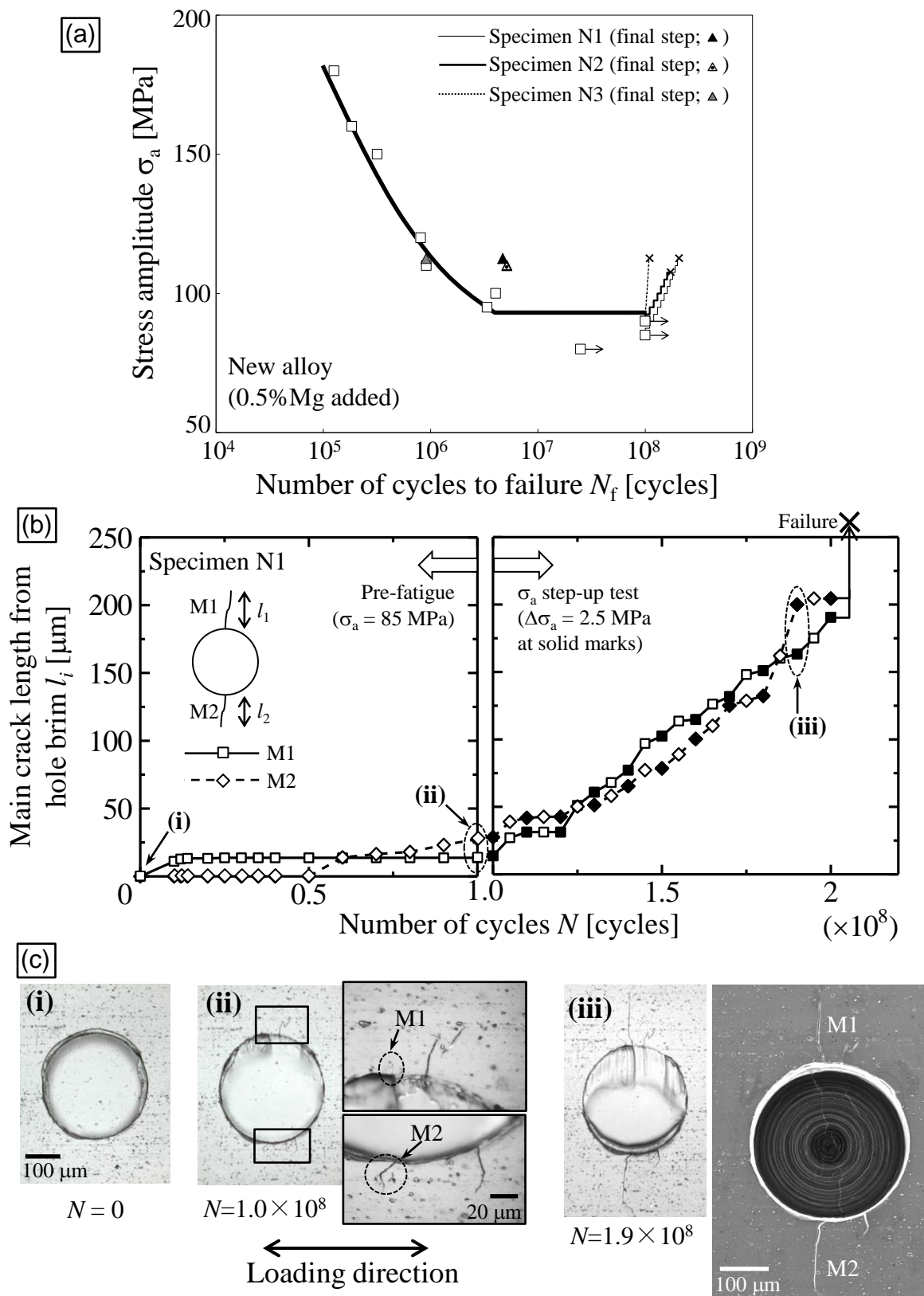

Fig. 13. Results of σ_a step-up tests for new alloy (0.5%Mg added): (a) fatigue history plotted on *S-N* diagram; (b) growth behavior of life-controlling main cracks (M1, M2) in specimen N1; (c) micrographs of main cracks in specimen N1.

Table(s)

List of Tables:

Table 1   Chemical composition of Al alloys (wt%) measured by ICP method

	Si	Fe	Cu	Mn	Mg	Cr	Ti	Zr	Al
Base alloy	0.52	0.20	0.20	0.09	0.95	0.23	0.02	–	bal.
0.5%Mg[*] added alloy	0.54	0.19	0.20	0.09	1.43	0.25	0.02	0.16	bal.
0.8%Mg[*] added alloy	0.55	0.23	0.22	0.09	1.92	0.25	0.02	0.14	bal.

* Nominal quantity

Table 2   Grain size, hardness, proof stress of Al alloys (after peak-aging treatment)

	Base	0.5%Mg added	0.8%Mg added
Grain size [μm] [*]	16.6	35.0	29.3
Vickers hardness [HV][**]	90.2	96.2	95.2
0.2% proof strength [MPa][***]	311	310	305

* Measured by intercept method; ** load value: 4 kgf (four point average), room temperature; *** strain rate: 5.6×10^{-4} s^{-1}, room temperature.

Table 3   Summary of σ_a step-up tests

Alloy	Specimen No.	Initial σ_a (MPa)	Initial cycles (cycles)	σ_a increment (MPa)	Cycles in one step (cycles)	Final σ_a at failure (MPa)	N_f at failure σ_a (cycles)
Base	B1	70	1.0×10^7	2.5	1.0×10^7	85	8.51×10^6
	B2	70	1.0×10^8			87.5	1.37×10^6
	B3	75	1.5×10^8			87.5	8.50×10^6
0.5%Mg added	N1	85	1.0×10^8	2.5	1.0×10^7	112.5	4.08×10^6
	N2	90			1.0×10^7	110	5.13×10^6
	N3	90			1.0×10^6	112.5	9.07×10^5

Table 4   Temperature/strain rate ranges for emergence of P–L effect in dilute alloys (Mg < 1%)

Mg content (wt%)	Temperature (K)	Strain rate (s^{-1})	Literature
0.5	R.T.	10^{-3} /10^{-4}/ 5×10^{-5}	Zhao et al. [38], Al-0.5%Mg
1.03	289 ~ 373	$< 10^{-2}$	Ogawa [23], 6061-O[*] (Si: 0.49%)
1.0	273 ~ 373	6.56×10^{-5}	Schwarz et al. [39], 6061-aq[**] (Si: 0.6%)
0.64	R.T.	4.39×10^{-4}	Cuniberti et al. [40], 6082-aq (Si: 0.5%)
0.5 ~ 1.0	R.T.	2×10^{-3}	Poole et al. [41], 6111-aq (Si: 0.6 ~ 1.1%)

*: annealed, **: as-quenched